Physics of the Earth and Planetary Interiors 263 (2017) 38–54

Contents lists available at ScienceDirect

Physics of the Earth and Planetary Interiors

journal homepage: www.elsevier.com/locate/pepi

Deformation-aided segregation of Fe-S liquid from olivine under deep Earth conditions: Implications for core formation in the early solar system

Madeleine T.L. Berg [a], Geoffrey D. Bromiley [a,b,*], Ian B. Butler [a], Mungo Frost [b], Robert Bradley [c], James Carr [c], Yann Le Godec [d], Laurent G.J. Montési [e], Wenlu Zhu [e], Kevin Miller [e], Jean-Philippe Perrillat [f], Elisabetta Mariani [g], Daniel Tatham [g], Simon A.T. Redfern [h]

[a] University of Edinburgh School of Geosciences, Grant Institute, King's Buildings, West Mains Road, Edinburgh, UK
[b] Centre for Science at Extreme Conditions (CSEC), King's Buildings, West Mains Rd, Edinburgh, UK
[c] Manchester X-ray Imaging Facility, School of Materials, University of Manchester, Oxford Road, Manchester M13 9PL, UK
[d] Institut de Minéralogie et de Physique des Milieux Condensés, UMR7590, Université Pierre et Marie Curie and CNRS, Paris, France
[e] Department of Geology, University of Maryland, College Park, MD 20742, USA
[f] Lab. De Géologie de Lyon, UMR5276, Université Claude Bernard Lyon 1, ENS de Lyon and CNRS, Villeurbanne, France
[g] Department of Earth, Ocean and Ecological Sciences, School of Environmental Sciences, University of Liverpool, 4 Brownlow Street, Liverpool L69 3GP, UK
[h] Department of Earth Sciences, University of Cambridge, Downing Street, Cambridge CB2 3EQ, UK

ARTICLE INFO

Article history:
Received 23 June 2016
Received in revised form 8 December 2016
Accepted 17 January 2017
Available online 19 January 2017

Keywords:
Core formation
Melt segregation
Mantle geochemistry
Deformation-aided percolation
Magma ocean

ABSTRACT

The planets and larger rocky bodies of the inner solar system are differentiated, and consist of metallic, iron-rich cores surrounded by thick shells of silicate. Core formation in these bodies, i.e. the segregation of metal from silicate, was a key process in the early solar system, and one which left a lasting geochemical signature. It is commonly assumed that extensive silicate melting and formation of deep magma oceans was required to initiate core formation, due to the inability of iron-rich melts to segregate from a solid silicate matrix. Here we assess the role of deformation in aiding segregation of core-forming melts from solid silicate under conditions of planetary deep interiors. Low-strain rate, high-pressure/temperature deformation experiments and high-resolution 2-D and 3-D textural analysis demonstrate that deformation fundamentally alters iron-rich melt geometry, promoting wetting of silicate grain boundaries and formation of extensive micron to sub-micron width Fe-rich melt bands. Deformation-aided Fe-S melt networks noted here contrast those observed in higher finite strain experiments conducted at lower pressure, and may reveal either an alternative mechanism for melt segregation at higher pressures, or an early stage process of melt segregation. Results suggest, however, that core-mantle chemical equilibration cannot be assumed in models of planetary formation, and that instead, the chemistry of rocky planets may record a complex, multi-stage process of core formation.
Crown Copyright © 2017 Published by Elsevier B.V. This is an open access article under the CC BY license (http://creativecommons.org/licenses/by/4.0/).

1. Introduction

Terrestrial bodies (rocky planets and larger asteroids) of the inner solar system are typically differentiated, consisting of metallic, Fe-rich cores surrounded by thick shells of silicate rock. Segregation of Fe-rich metal from silicate was, therefore, a defining process in the formation of the rocky planets, and one which has likely left a lasting geochemical signature. Fe-rich liquids melt at considerably lower temperature than silicate, 1213–1233 K compared to 1450–1850 K (Sahijpal et al., 2007), giving a potentially substantial time-frame in accreting rocky bodies during which core-forming Fe-rich metals were in liquid form whilst the silicate portion was largely solid. Constraining the interconnectivity and permeability of such melts within a solid silicate matrix is, therefore, key to understanding the processes, timing and chronology of core formation in the early solar system.

Over the last two decades a significant number of petrologic experiments have been conducted at various pressures, temperatures, compositions and timescales to determine the permeability of metallic melts (Fe ± Si, Ni, S, O) in a pure olivine or peridotitic matrix (e.g. Linnen and Keppler, 1997; Shannon and Agee, 1996; Shi et al., 2013; Terasaki et al., 2007). 3-D permeability has traditionally been estimated from 2-D quench textures using dihedral angle (solid-solid-melt) measurements (Von Bargen and Waff,

* Corresponding author at: University of Edinburgh School of Geosciences, Grant Institute, King's Buildings, West Mains Road, Edinburgh EH9 3FE, UK.
E-mail address: geoffrey.bromiley@ed.ac.uk (G.D. Bromiley).

http://dx.doi.org/10.1016/j.pepi.2017.01.004
0031-9201/Crown Copyright © 2017 Published by Elsevier B.V.
This is an open access article under the CC BY license (http://creativecommons.org/licenses/by/4.0/).

1986). A dihedral angle of >60° means the system is impermeable below a certain threshold melt fraction (known as the pinch-off melt fraction), which increases with increasing dihedral angle. A value of <60° theoretically implies melt remains interconnected until the solid is completely drained. The vast majority of studies on olivine-metallic liquid systems have found that when left to anneal to textural equilibrium, dihedral angles are consistently >60 ° (Shannon and Agee, 1996; Terasaki et al., 2007), with the pinch-off melt fraction determined by Yoshino et al. (2003) to be 5%, >6% by Watson and Roberts (2011), between 6 and 9.5% by Terasaki et al. (2005), and possibly even higher (Bagdassarov et al., 2009; Walte et al., 2007). This implies that core formation by percolation would have been highly inefficient, and left a significant fraction of Fe-rich melt trapped within the silicate portion of rocky bodies, inconsistent with many aspects of the observed geochemistry of the bulk-silicate Earth, including the concentration of highly siderophile elements (HSE) (Minarik et al., 1996). As such, it is widely believed that substantial silicate melting, and the formation of extensive 'magma-oceans' in which immiscible Fe-rich and silicate liquids could readily and efficiently separate, would have been required to initiate core-formation in rocky planetesimals, planets and large asteroids (Ringwood, 1979).

Magma ocean models for core-formation imply some degree of chemical equilibration between liquid silicate and liquid metal, often assumed to be full chemical equilibration under the conditions of the base of a deep silicate magma ocean (e.g. 44 GPa, >3000 K (Wood et al., 2008)). However, although models such as the one presented by Wood et al. (2008) can explain some aspects of the observed geochemistry of the bulk silicate Earth (BSE) they still require a rebalancing of the BSE HSE content, assumed to occur during a late heavy bombardment accretionary event (Touboul et al., 2015). Such high-pressure/temperature (HPT) segregation of metallic and silicate liquids should result in isotopic fractionation; however, this is notably not observed in high-resolution studies of Fe isotopes (Craddock et al., 2013; Halliday, 2013). There is also a growing realisation that many smaller rocky bodies in the inner solar system are also fully differentiated, and whilst long-lived deep magma oceans may be sustained on larger bodies, this is more difficult to justify on smaller bodies which lose heat to space more efficiently and which have considerably smaller accretionary profiles. For example, it has been suggested that the parent body for Ureilite meteorites differentiated at low temperatures (<1373 K), before the onset of silicate melting (Barrat et al., 2015). An efficient, alternative mechanism for core-formation in planetesimals remains, however, elusive.

Previous experiments on segregation of Fe-rich liquids from solid silicate are largely based on HPT experiments performed under hydrostatic conditions. However, vigorous convection in hot, accreting bodies and the effects of continuous bombardment and gravitational settling are likely to have resulted in very dynamic (i.e. non-hydrostatic) conditions in rocky bodies in the early solar system, precluding the development of the type of fully equilibrated textures studied in traditional hydrostatic HPT experiments (Rushmer et al., 2005). In recent years a number of studies have focused on metallic liquid/solid silicate segregation in dynamic systems, and concluded that non-uniaxial stresses can significantly alter melt geometry and promote wetting of grain boundaries, creating interconnected metallic melt networks in systems in which melt otherwise remains trapped under static conditions (Bruhn et al., 2000; Groebner and Kohstedt, 2006; Hustoft and Kohlstedt, 2006; Rushmer et al., 2005). In dynamic 2-phase solid/melt systems undergoing deformation, differential stress clearly has a significant effect on melt permeability. Melt migration can continue to progress as long as the differential stress acting to force melt along grain boundaries exceeds the effect of interfacial tension, which otherwise acts to isolate melt pockets at triple junctions (Groebner and Kohstedt, 2006). The pinch-off melt fraction in dynamically deforming systems is, therefore, likely to be very much reduced relative to that in static, texturally equilibrated systems (Hustoft and Kohlstedt, 2006), and as a consequence of these factors, such 'deformation-aided segregation' has been proposed as an alternative, efficient mechanism for core-formation in planetissimals prior to, or in the absence, of extensive silicate melting. However, due to limitations in experimental equipment, few deformation studies have been conducted under realistic conditions of core formation in planetary interiors. Aside from the issue of strain rate, which by necessity is orders of magnitude faster in experiments than in natural systems, it can be argued that the experiments of Rushmer et al. (2005) were conducted in a bulk composition not applicable to segregation in larger planets and in systems with high, already interconnected, melt fractions, and the experiments of Hustoft and Kohlstedt (2006) at too low confining pressure. Walte et al. (2011) provided the first assessment of the influence of strain rate on metallic liquid segregation directly under realistic HPT deep planetary conditions, and suggested that differential stress becomes too low to create interconnected melt networks between small melt pockets at lower strain rates. However, interpretation of high-pressure run products by Walte et al. (2011) is partly dependent on experiments performed in a low-pressure analogue system, and importantly, the experimental geometry of axial compression which they used in their D-DIA experiments arguably cannot promote the same melt segregation mechanism and development of channelized melts observed in previous lower pressure studies.

An additional area of uncertainty in previous studies lies in 3-D textural analysis. The majority of studies have relied on dihedral angle measurements to extrapolate from textures observed in 2-D to estimates of 3-D connectivity and permeability. Non-hydrostatic experiments preclude the attainment of textural equilibrium, and deformed experimental samples are shown to be texturally heterogeneous and complex, meaning dihedral angles cannot be used to predict 3-D melt geometry (Groebner and Kohstedt, 2006). Permeability and connectivity in such samples is, in essence a 3-D geometric feature, and the ability to characterise melt geometry in 3-D is crucial to constraining these characteristics. The advancement of X-ray Computed Tomography (XCT) provides a non-destructive method to visualise the interior of partially molten samples directly using laboratory and synchrotron X-ray sources. Watson and Roberts (2011) performed 3-D reconstructions of Fe-rich melts in solid olivine systems under hydrostatic conditions, although textural interpretation in that study was limited due to resolution limitations of standard micro-CT approaching the size of features observed in samples.

The aim of this study is to carry out controlled, very low strain rate (10^{-6} s^{-1}) torsional deformation experiments under realistic high P-T conditions for core formation in planetesimals to provide insight into the efficiency of deformation-aided percolation. In addition to traditional 2-D sectioning and analysis, we also characterise textures in quenched samples using both micro- and nano-resolution XCT. This permits both assessment of the merits and limitations of 2-D and 3-D analysis, and of the capability of recent advances in 3-D imaging techniques to provide insight into textural development in complex, fine-grained geological systems.

2. Methods

2.1. Starting materials and HPT experiments

Experimental samples were prepared from powdered gem-quality, inclusion-free olivine (Fo_{89}) from Åheim, Norway and powdered synthetic troillite (FeS, making up 4% by volume of the total

mixture) and combined by grinding under ethanol, creating a fine grained (<30 μm) homogeneous starting mixture. An early series of experiments (FeOlPC1-6, FeOl1, FeOlcam1, FeOlcam2) were carried out using a starting mixture of olivine +4 vol% Fe_3S (as a mechanical mixture of Fe metal and troilite). This starting material was of a more variable grain size. Deformation experiments were performed using the rotational Paris Edinburgh Cell (roPEC, Fig. 1), either off-line at the Dept. Earth Sciences, University of Cambridge, or installed on the extreme conditions ID27 beamline at the European Synchrotron Research Facility (ESRF), Grenoble, France. This device allows controlled, variable strain and strain rate torsional deformation at simultaneous high P-T (Bromiley et al., 2009). In all experiments, pressure was increased at a rate of 5 bars/min to 3 GPa. Once pressure had stabilized, temperature was then increased at a rate of 10–100 °C/min to the final run temperature. Samples were left to anneal for at least 2 h to relieve sample strain accumulated during initial compression. Time-series piston-cylinder experiments demonstrate that 2 h was sufficient to equilibrate the olivine + FeS sample, and produce a texture of recrystallized olivine with FeS trapped at grain boundaries, as discussed below. Following this initial annealing, samples were then deformed in torsion by rotating the upper anvil at controlled strain-rates. Initial calibration of pressure and temperature was carried out by in-situ X-ray diffraction of MgO and Pt at the ESRF (Bromiley et al., 2009; additional unpubl. data). Off-line experiments used these calibrations, applying the same power and pump pressure values, with a predicted error range of ±1 kbar for pressure, and ±50 °C for temperature. For in-situ experiments, P and T were determined in-situ from powder diffraction data of internal calibrants (MgO and Pt). Sample deformation in off-line experiments was measured during experiments by a digital measure of anvil rotation, and confirmed after the experiments had been recovered by examination of internal platinum strain markers. Run conditions for all experiments are given in Table 1. A comparison of strain-rate and total strain in our experiments (maximum strain determined at the edge of samples) compared to those of previous studies, typically performed at greater finite strains and strain rates, is shown in Fig. 2. The most comparable study is that of Walte et al. (2011), which is also conducted at high pressures (3 GPa). It is important to note, however, that the Walte study was conducted under uniaxial compression, while our torsional equipment allows us to examine the effects of simple shear on the system.

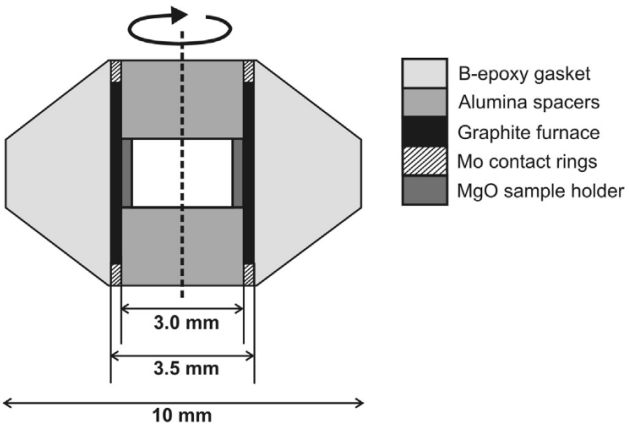

Fig. 1. roPEC sample assembly used for deformation studies. Assembly sits between two opposed carbide anvils in the roPEC press frame, as described in Bromiley et al. (2009). Pressure is achieved by compressing the assembly, with the gasket supporting the load from the anvils. High temperatures are achieved by passing a current through the graphite resistance furnace. Rotation of the upper anvil relative to the stationary lower anvil imparts a torque on the entire assembly, including the sample.

Control experiments were performed under hydrostatic conditions using end-loaded piston-cylinder apparatus and a high-temperature talc-Pyrex-graphite assembly (see Bromiley et al., 2010; Bromiley and Hiscock, 2016, for details). The starting mix was loaded into 4 mm o.d. graphite capsules which were inserted into alumina sleeves and then loaded into the sample assembly. Experiments were pressurised and then slowly heated (100°/min) to the final run temperature. Temperature was measured using an R-type thermocouple adjacent to the capsule, and both temperature and pressure were monitored and maintained throughout the experiment. Samples were quenched by switching off power to the heating circuit whilst maintaining run pressure (quench rates >100°/s). Run conditions are given in Table 1.

2.2. X-ray tomography

XCT was used to provide a 3-D model of melt structures in recovered samples prior to later sectioning. The 2-phase Fe-rich melt/olivine system is well suited to XCT investigations due to clear differences in X-ray absorption (attenuation) of the main phases. Preliminary scans were made using the X-ray CT system built in-house within the Experimental Geosciences Facility, School of Geosciences. 1000 projections were made on a 360° rotation of samples at an X-ray energy of 100 kV, averaging three 1s exposures at each projection. A copper foil filter was used to reduce beam hardening artefacts. Cone beam data was reconstructed using the University of Ghent's Octopus™ software to produce 3D images at ~2 μm voxel size. Additional scans were performed at the Manchester X-ray Imaging Facility (HMXIF) on the Zeiss Xradia Versa scanner. 2001 projections were made over a 360° rotation of the sample, at 80 kV and 35 s exposure. A Low Energy filter (LE# 1) was used to reduce beam hardening artefacts. Samples were cut and polished to 1x1 mm matchsticks or prepared as 15×15 μm slices by focused ion beam to maximize resolution. Slices were reconstructed using the Zeiss Xradia XM reconstructor software to produce 3-D images at 1 ± 0.2 μm voxel size. Nanotomographic scans were carried out on the Zeiss Xradia Ultra-810 equipment at HMXIF, in which a sample was scanned at 0.13 μm voxel size with a 65 μm field of view. An additional scan of 50 nm voxel size was carried out on a 15 μm sub-section of deformed sample FeOl1. A summary of tomographic scans is given in Table 1.

2.3. High-resolution 2-D textural analysis

Qualitative and quantitative textural analysis was conducted on cut and polished sections in order to ground-truth interpretation of reconstructed tomographic slices and provide high-resolution textural analysis. Samples were cut in three orientations to allow examination of textures: two perpendicular cross-sections and a tangential slice to view an area affected by simple shear of known orientation. Sections were studied using a Philips XL30CP Scanning Electron Microscope at the Edinburgh Materials and Micro-Analysis Centre (EMMAC), School of GeoSciences, University of Edinburgh. Backscatter Electron (BSE) images were used as well as the inbuilt PGT Spirit X-ray analysis system, in order to distinguish between phases during initial analysis. In addition, Electron Backscatter Diffraction Analysis (EBSD) was carried out on polished sections of quenched samples in order to assess the effect of low degrees of deformation on olivine crystal preferred orientation and deformation of individual crystals, in dry and partially molten systems. Finally, quantitative analysis and element mapping was carried out on the CAMECA SX100 Electron Microprobe (Edinburgh Materials and Micro-Analysis Centre) to determine diffusion of iron or other elements between metal and silicate components

Table 1
Experimental conditions used in static and deformation studies and details of XCT sample characterisation.

A. Sample	Composition	T/°C	Anneal time/min	Tomographic analysis
FeOlPC1	Ol + 4 vol% Fe_3S	1050	120	
FeOlPC2	Ol + 4 vol% Fe_3S	1100	480	
FeOlPC3	Ol + 4 vol% Fe_3S	1100	1710	
FeOlPC4	Ol + 4 vol% Fe_3S	1450	2820	Micro-CT (2 μm)
FeOlPC5	Ol + 4 vol% Fe_3S	1300	1650	Micro-CT (2μm)
FeOlPC6	Ol + 4 vol% FeS	1100	2790	
FeOlPC8	Ol + 4 vol% FeS	1350	2880	Micro-CT (2 μm) Nano-CT (0.13 μm)

A. Sample	Composition	T/°C	Anneal time/min	Tomographic analysis	Time under strain/min	Rotation/°	Strain rate/$s^{-1,*}$
FeOl3	Ol + 4 vol% Fe_3S	1100	120		720	40	8.0E−6
FeOl-Cam1	Ol + 4 vol% Fe_3S	1400	120	Micro-CT (2μm)	180	60	5.0E−5
FeOl-Cam2	Ol + 4 vol% Fe_3S	1600	120		120	80	1.0E−4
Cam3-FeOl1	Ol + 4 vol% FeS	1450	120	Micro-CT (2μm) Nano-CT (0.13μm) Ultra-nano-CT (0.05μm)	1420	53	1.7E−6
Cam3-FeOl2	Ol + 4 vol% FeS	1450	120	Micro-CT (2μm)	200	75	1.7E−5
Cam3-FeOl3	Ol + 4 vol% FeS	1450	120	Versa Micro-CT (1μm) Nano-CT (0.13μm)	530	119	1.0E−5
Cam3-FeOl4	Ol + 4 vol% FeS	1450	120	Versa Micro-CT (1μm)	605	90	6.9E−6

* Maximum strain determined at edge of deformed samples.

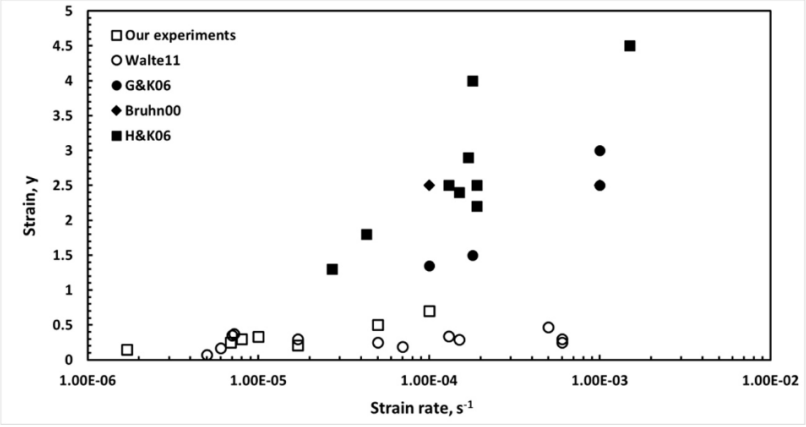

Fig. 2. Conditions used in this and previous studies of the effect of deformation on textural development in silicate-metallic melt experiments. Walte11: Walte et al. (2011), G&K06: Groebner and Kohstedt (2006), Bruhn00: Bruhn et al. (2000), H&K06: Hustoft and Kohlstedt (2006). Note that Walte et al. (2011) compressed samples axially, compared to simple shear geometry used in other studies, so determined finite shear is not strictly comparable.

during experiments and ensure no significant reaction was taking place between the sample and surrounding MgO capsule (see supplementary material).

3. Results and discussion

3.1. 2-D textural analysis

Undeformed olivine/Fe-S melt samples contain, as expected, isolated melt pockets which pinch out at a high angles at grain boundary triple junctions (Fig. 3A–C). The 2-D texture suggests melt is isolated and trapped at triple junctions within the olivine matrix, and dihedral angle analysis is in agreement with previous studies (Shannon and Agee, 1996) with median values of 80° (i.e. significantly exceeding 60°). After an annealing time of 2 h, textures are well developed with no evidence for melt interconnectivity; no significant changes in texture are noted after prolonged annealing of several days. Distinct differences in texture are noted in deformed samples (Fig. 4); observed textures are also different across the three samples cut for SEM analysis (Fig. 5). Melt is generally more finely distributed across smaller melt pockets in deformed samples, which are not limited to grain boundary triple junctions, as also noted in the high-pressure deformation studies of Walte et al. (2011) and Cerantola et al. (2015). Melt veins of a range of sizes and extents are also present in each sample and melt is seen wetting grain boundaries in thin (sometimes <0.1 μm) sheets. These fine sheets are seen to connect larger melt pockets across multiple olivine grains connecting across distances of up to several hundred microns. Melt distribution is more variable across the deformed samples, with areas of significant melt accumulation, as well as areas that are relatively 'drained' of melt populated with very fine near-spherical melt pockets (Fig. 5). This indicates that there has been some localised redistribution of melt into melt-rich and melt-poor zones over the duration of the experiments. SEM analysis of samples FeOl3 and FeOl-Cam1 and FeOl-Cam2 also reveals the presence of melt channels and extensive wetting of olivine grain boundaries by Fe-S melt. However, the more variable Fe-S grain size used in the starting mix for these earlier experiments means that textures due to melt redistribution and accumulation are more difficult to interpret, and small melt channels are additionally formed by hydraulic fracturing across olivine grains

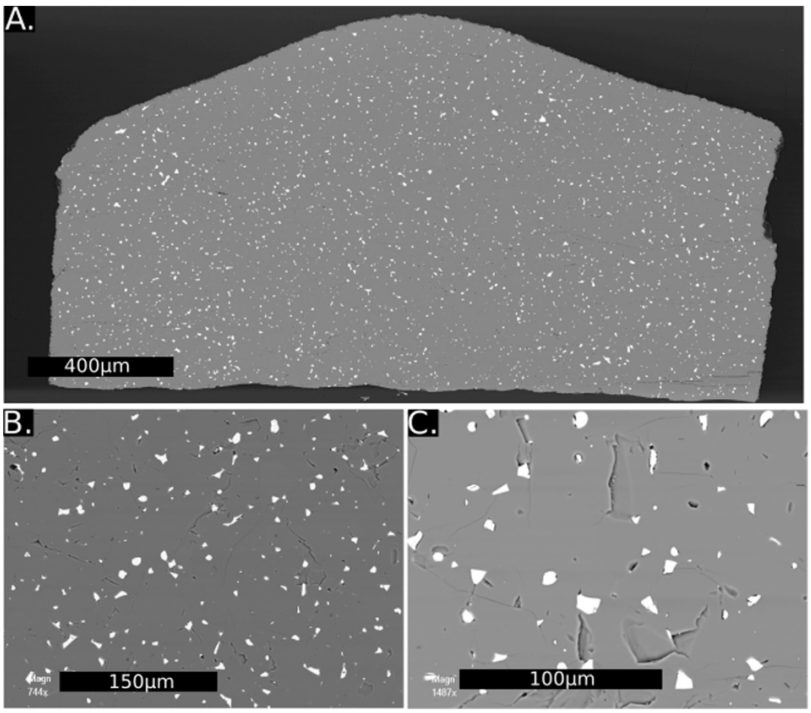

Fig. 3. Back-scattered electron (BSE) SEM images showing distribution of Fe-S quenched melt (white) within solid olivine (silicate) matrix (grey) from PCFeOl8, annealed under static conditions. Melt phase is clearly trapped at grain junctions, with a high dihedral angle strongly indicative of isolated, non-connected, melt pockets. Spherical melt pockets indicated melt trapped within olivine grains due to grain growth. Black bar for scale. Arrows indicate sense of shear in deformed samples.

adjacent to larger Fe-S melt pockets. Therefore, although these samples provide further evidence of the efficiency of deformation-aided Fe-S melt percolation, textures in these samples are not considered further here.

The largest melt vein is observed on a planar cut within Cam3-FeOl1, which is interconnected over a length scale >300 µm and is 100 µm wide. Qualitatively, there does not appear to be a systematic change in melt textures, or frequency of interconnected melt veins across sections in any of the orthogonal sections observed, including planar and cross-sectional sections which theoretically represent a change from maximum shear at the edges, to zero stress/strain at the centre. Although wetting of olivine grain boundaries and the presence of Fe-S melt bands is noted in all deformed samples, the described features are significantly more widespread and clearly developed in our longest duration (lowest strain-rate) experiment. Fig. 5 shows examples of melt textures within Cam3-FeOl1. Although melt veins are present in each of the deformed samples, they are not as widespread in the sections cut from Cam3-FeOl2 and Cam3-FeOl4 (Fig. 4), although melt in these samples is more finely distributed in than in undeformed samples and again shows evidence for localised remobilisation.

On tangential and mid-section cuts it is possible to see that larger melt pockets in deformed samples are aligned sub-horizontally, i.e. sub-parallel to the direction of applied shear stress. The exact orientation of these melt accumulations appears to vary from the edges (high strain) to the centre (low strain) of the samples. In order to assess the strength and orientation of any fabric within experimental samples, auto-correlation function (ACF) analysis was carried out on 2-D sample sections using the ImageJ™ plugin Jazy ACF (Heilbronner and Barrett, 2014). The auto-correlation function describes the heterogeneity of an image by comparing it to a direct copy of itself, at varying displacement from its original position. In the undeformed samples ACFs are random across the sample, as would be expected for a relatively isotropic fabric (Fig. s8). Large ACFs in deformed samples are generally aligned between 0–30° and 150–180°, i.e. at low angles to the horizontal, implying a weak fabric created sub-horizontal to the shear direction (Fig. s8). Sample Cam3-FeOl1 shows a change from high angles on the left edge, to low angles on the right, with horizontal alignment in the centre, which may be an indication that the fabric orientation is changing in response to the maximum stress orientation (which is in opposite directions at either end of the sample and at a minimum in the centre). Hustoft and Kohlstedt (2006) noted the development of more extensive Fe-S melt-rich bands in deformed polycrystalline olivine at angles of approximately 18° to the shear plane, although we note here that alignment is only observed in larger melt pockets, and is not immediately apparent in finer melt channels.

3.2. 3-D textural analysis from micro-XCT

Micro-XCT analysis conducted at the University of Edinburgh was used to produce datasets ranging in voxel size of 2–3 µm for 2 mm field of view (FOV), whole-sample scans. Although this voxel size is coarse in comparison to textures observed in quenched sections, the ability to image whole sample volumes means that data can be used to provide information on: (1) melt volume distribution throughout samples, and evidence for melt migration as a response to gradients in pressure/temperature/strain within the samples; and (2) Orientation of fabrics produced in response to the orientation of stress tensors and changes in magnitude of stress across deformed samples. 3D reconstructions of four deformed and one undeformed samples are shown in Fig. 6. As observed in 2-D images, melt distribution is more variable in the deformed samples, with a fabric created by alignment of larger melt pockets, although there are also variations in melt distribution observed across the undeformed sample. Partial volume effects are significant in these micro-XCT scans, caused by relatively large voxel size relative to size of textural features. This means that large volumes segmented as the melt phase are likely to be a combination of fine

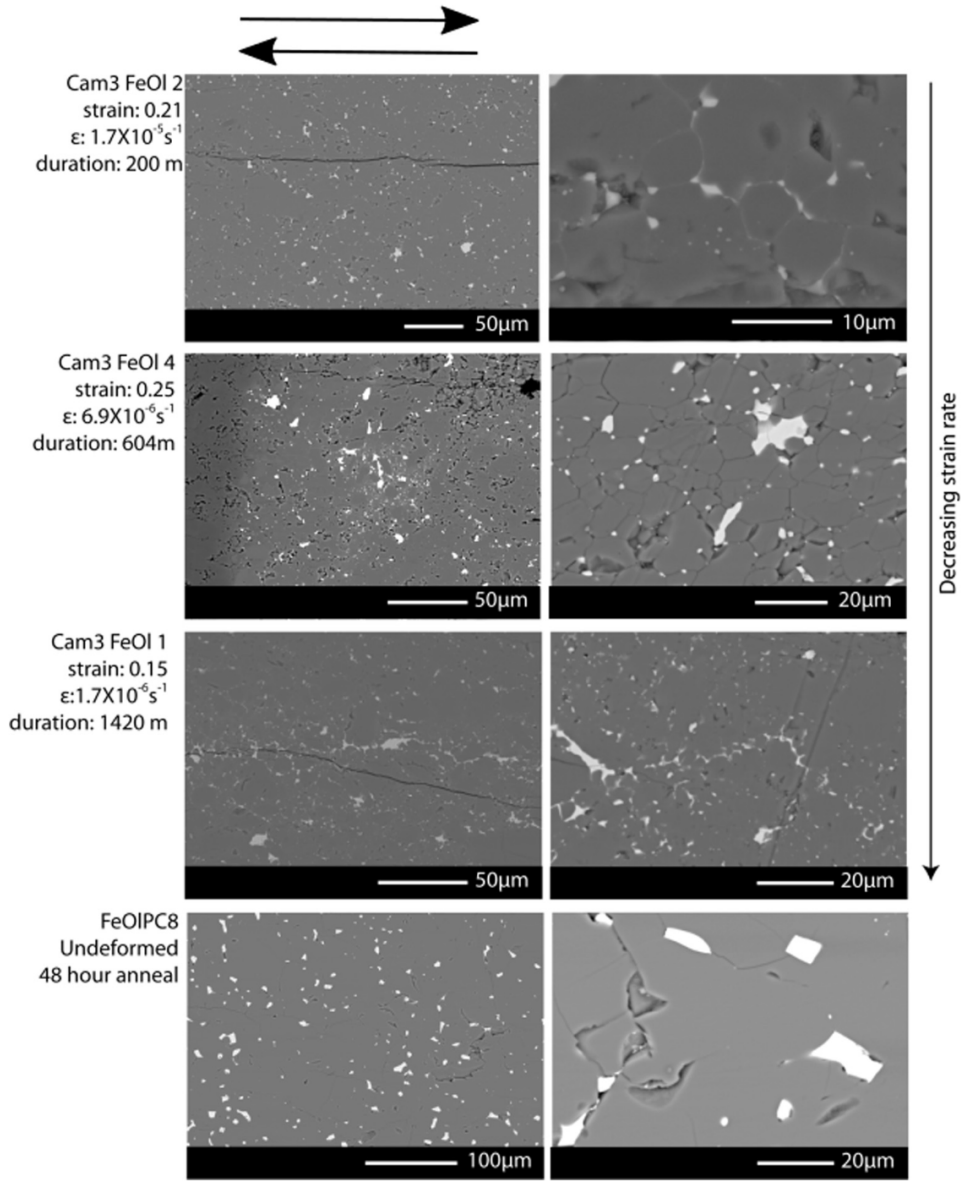

Fig. 4. BSE SEM images showing examples of textures in undeformed and deformed run products (experimental conditions labelled).

melt veins surrounding small olivine grains, as observed in 2-D textures, rather than single large melt pockets. These large volumes still represent areas of higher melt %; analysing their distribution can, therefore, give information about potential localised segregation into melt-rich and melt-poor regions. To quantify melt distribution, the volume % of the segmented melt phase was calculated from segmented images per slice in X, Y, and Z directions as shown in Fig. 7, where Z is the vertical axis (direction of pressurisation) and X and Y are in the shear plane (i.e. in the direction of shear). Overall the undeformed sample appears slightly less variable than deformed samples, particularly in the Z direction, although the difference is subtle. FeOlPC8 does show an inherent variability although the range of volume % are small in the X and Z directions, and the variability appears to be in broader peaks, especially in the Z-direction, suggesting a more gradual increase and decrease in melt % over a larger area, possibility related to variations in the starting mixture. Cam3-FeOl1 shows very high variability, particularly in the Z and Y directions. There is a clear peak of melt% in the central portion of the sub-volume examined, both in Z and X directions, possibly due to the tendency for melt to move to the central (undeformed) region of samples. Other deformed samples do not show significant variation in volume distribution, particularly in the X and Y direction, and in FeOl2 melt appears to be more finely distributed than in the undeformed sample, showing no sign of melt accumulation or migration. This is consistent with qualitative observations; although there is evidence for localised mobilisation of melt, there is no evidence for large-scale melt migration across the samples.

Although Micro-CT analysis can reveal evidence for change in melt distribution across samples, there is an obvious limitation to the usefulness of data at this resolution. SEM images reveal a very fine distribution of melt, particularly within deformed samples, where melt sheets of less than 1 µm are ubiquitous. These cannot be visualised successfully with a voxel size of 1–3 µm. Par-

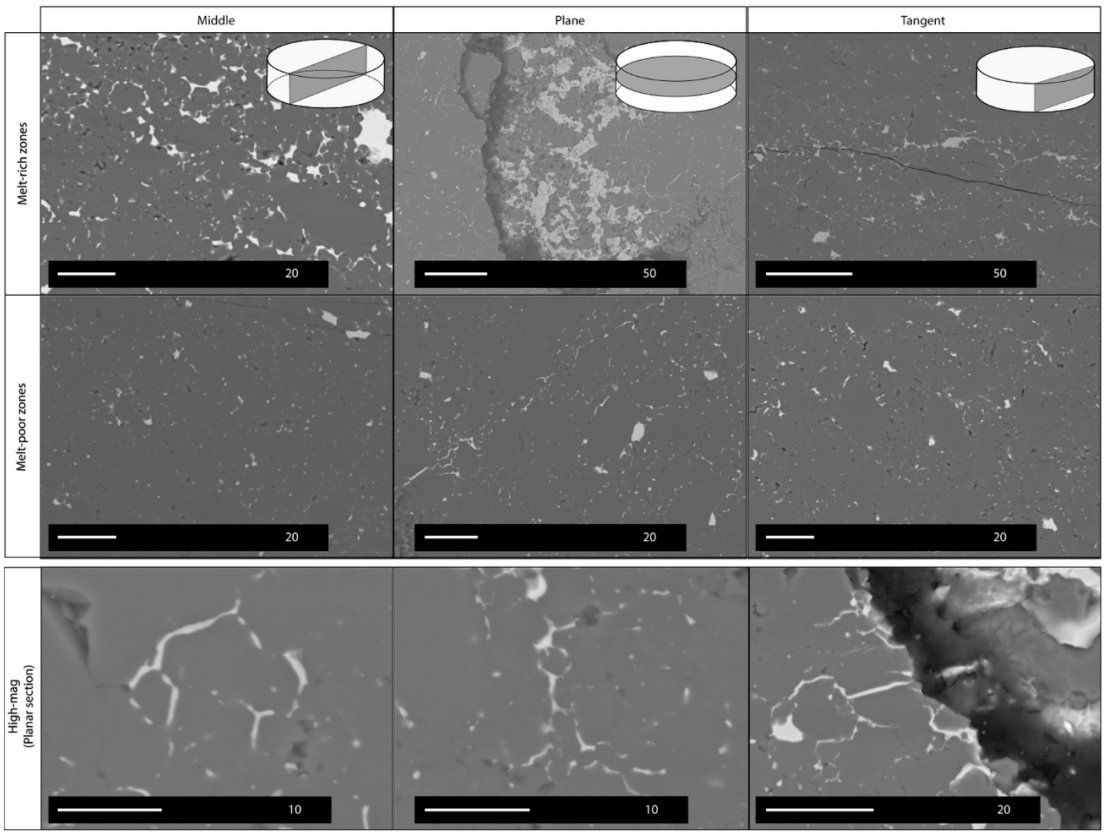

Fig. 5. Examples of textures developed in sample Cam3-FeOl1, the longest duration, lowest strain-rate sample (24 h duration, 10^{-6} s^{-1}, deformed to ~90° in torque). Examples of melt-rich veins and relatively drained areas are shown in middle, planar and tangential cuts. The lower row of images shows high magnification examples of wetted olivine grain boundaries with melt sheets 1 μm or less. The bottom right image is of melt veins close to a larger melt vein (see planar melt-rich zone) and exhibits small melt filled fractures within olivine crystals. These only develop close to the largest melt accumulations. The large crack associated with the very large melt accumulation is most likely a post-quench decompression feature localised around the melt vein/silicate boundary.

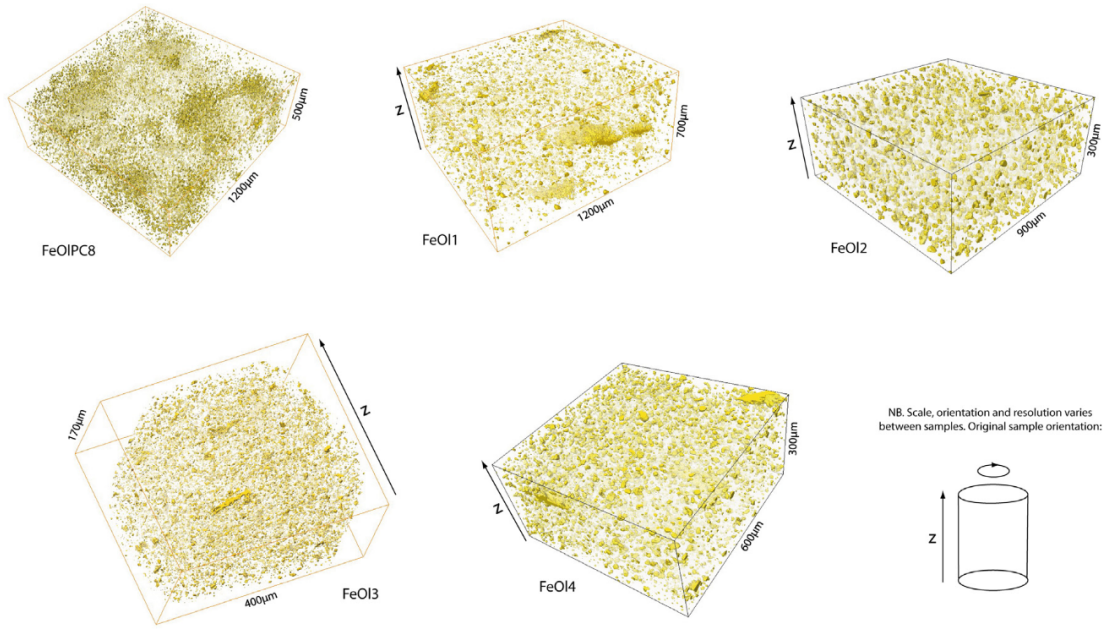

Fig. 6. Volume renderings of Fe-rich melt (gold) in micro-CT reconstructions of undeformed sample (FeOlPC8) and deformed samples Cam3-FeOl1-4. Olivine matrix has been rendered transparent for clarity. Orientation of the sample Z axis (parallel to torsional axis of rotation) is shown by arrows to orient each deformed sample. 2 μm voxel size. (For interpretation of the references to colour in this figure legend, the reader is referred to the web version of this article.)

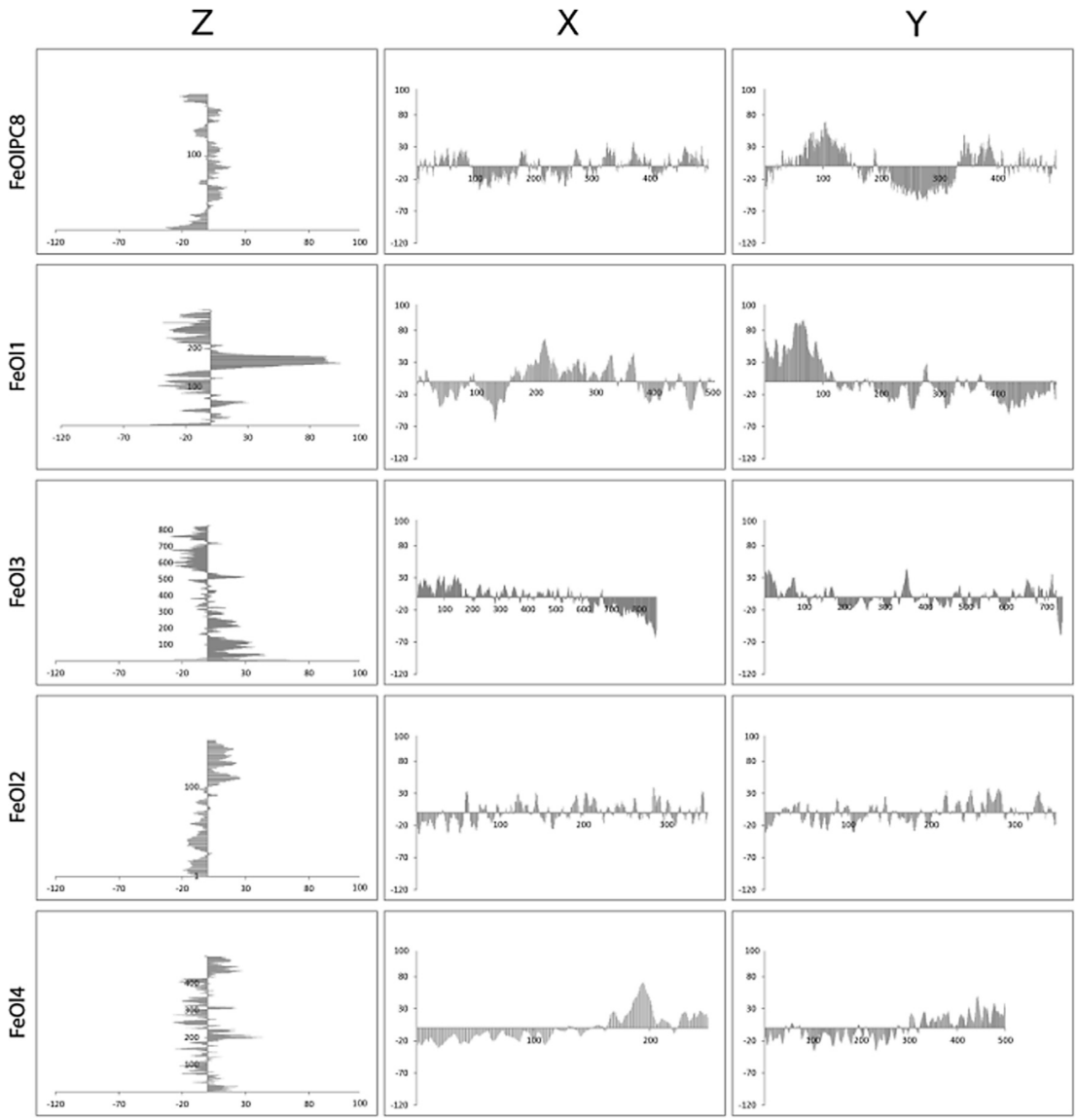

Fig. 7. Relative melt distribution across the sample in terms of volume percentage of melt present across slices in three orthogonal directions for samples Cam3-FeOl1–4, and undeformed FeOlPC8. Extracted area % of melt phase determined using Avizo Fire™ 'material statistics' function, following noise reduction and application of a minor smoothing filter, and segmentation of melt phase. To allow comparison between samples, data are converted to % change in the whole sample volume. Z direction is the original orientation of slices (see Fig. 6). Orthogonal X and Y directions have been chosen to ensure slice area is similar across samples, as the area of the slice analysed will affect variability of volume distribution. For Z direction (graph on left), vertical axis is slice number, and X axis represents % change from average volume fraction of the whole sample – in X and Y directions (middle and right-hand graphs) these axes are inverted.

tial volume effects will act to 'smear out' these fine features changing both volume and shape and making them essentially impossible segment.

3.3. Melt geometry and connectivity from nano-XCT

Nano-resolution XCT scans were carried out on small subvolumes of samples Cam3-FeOl1, Cam3-FeOl3 and undeformed FeOlPC8, for 65×65×65 μm sample volumes with a 130 nm voxel size, and one ultra-nano scan of FeOl1 at 15×15×15 μm sample volume, 50 nm voxel size. Volumes were taken approximately 2/3 the distance towards the outer edge of the samples to ensure sample volumes did not include any features due to proximity with the MgO sample container, but were otherwise not preselected based on features observed during lower resolution imagining. Slices were filtered using non-local means filtering, then segmented by binarising the greyscale data into melt and non-melt areas using a combination of simple global thresholding (to segment data based on strong differences in X-ray attenuation between the Fe-S and olivine phases) and watershed segmentation. Interpretations are additionally ground-truthed by extensive SEM investigation of the samples. Resolution of these scans is high enough to allow much improved phase segmentation with a smaller partial volume effect, allowing melt pocket shape and volume to be estimated more accurately, and confirming the presence and revealing the topological detail of 3-dimensional Fe-S melt networks along wetted grain boundaries within the olivine matrix. Although representative of only small volumes of the samples, textures observed can be ground-truthed by larger scale CT scans and 2-D BSE analysis.

Nano-CT scans highlight the difference in textures between deformed and undeformed samples (Fig. 8). Particle shape within

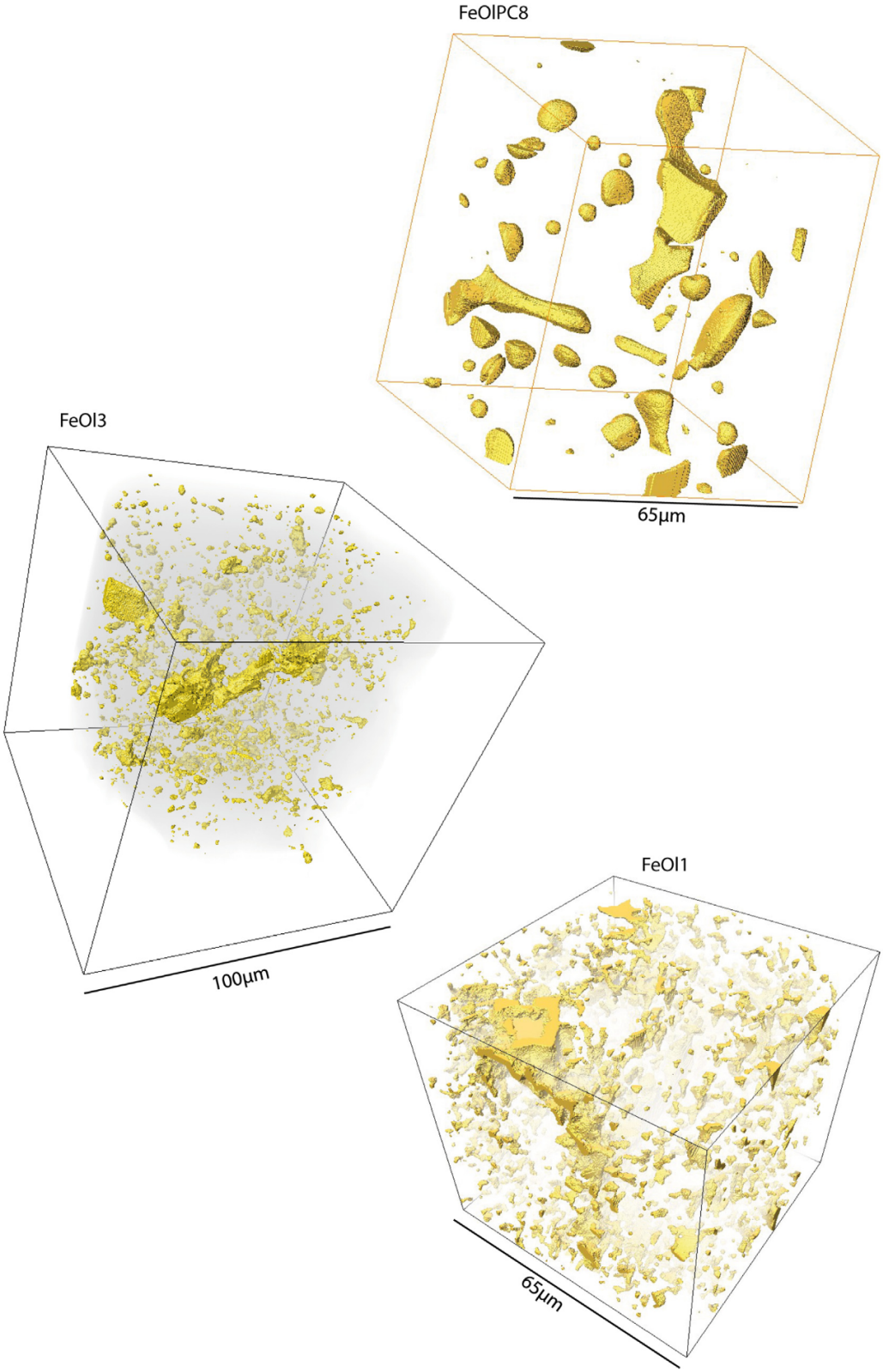

Fig. 8. Reconstructions of Fe-S melt (gold) from nano-XCT scans. Olivine is rendered transparent (faint grey in FeOl3 to show sample outline). FeOlPC8 is an undeformed sample while FeOl3 and FeOl1 are deformed. Vertical axis in reconstructions is parallel with the z axis shown in Fig. 6. 0.13 µm voxel size. (For interpretation of the references to colour in this figure legend, the reader is referred to the web version of this article.)

undeformed FeOlPC8 is relatively uniform, and melt pockets are close to spherical with clear angular edges on melt pockets representing the melt pinching off at high dihedral angles to the olivine grains, consistent with 2-D high resolution SEM imaging. Smaller spherical particles are likely to represent melt trapped within olivine grains that have grown during annealing, which was also observed in SEM analysis. In deformed samples, melt particles have less uniform shapes, most showing a more concave nature with convolute margins and narrower sheet-like structures. Even at this fine scale it is clear that the melt within deformed samples, although distributed more finely overall, also accumulates to form large melt pockets or sheets. In the case of Cam3-FeOl1, one of these melt sheets stretches diagonally from one end of the scanned volume to the other – its total length within the volume is around 100 μm, but the extent of the melt network is likely to be greater. A reconstruction of this large interconnected melt pocket is shown in Fig. 9. It is possible to see very fine individual melt sheets joining together to connect two larger melt accumulations. Fine melt sheets are likely to represent melt wetting olivine grain boundaries, connecting together to form a network of sheet-like veins. Small isolated melt pockets are still present within sample volumes, but they represent a smaller proportion of total melt than in the undeformed sample. Sample Cam3-FeOl3 shows similar melt geometry and volume distribution, but there is no large interconnected melt pocket/channel cutting across the volume of the sample studied, and overall there are fewer large melt pockets. A larger proportion of the melt is trapped in isolated pockets, most likely due to the small sampled volume having been relatively drained of melt. This highlights the importance of conducting both larger volume/low-resolution and smaller volume/high resolution 3-D analysis when assessing textures in complex materials, but also highlights the current technical issues in performing very high resolution 3-D textural analysis of such samples. It is clear from this study that textures in this simplified 2-phase system are complex and heterogeneous on varying length scales. The fine-structure of melt pockets and channels, which range down to less than 100 nm, requires very high-resolution 3-D image analysis which can only be conducted on small sub-volumes of material. In order to gain an accurate understanding of textural development, such high-resolution analysis needs to be conducted on much larger volumes of the samples, in order to ensure that sampled regions are representative of the entire sample volume. This would require analysis of multiple slices of each sample, which is both technically challenging and prohibitively time-consuming.

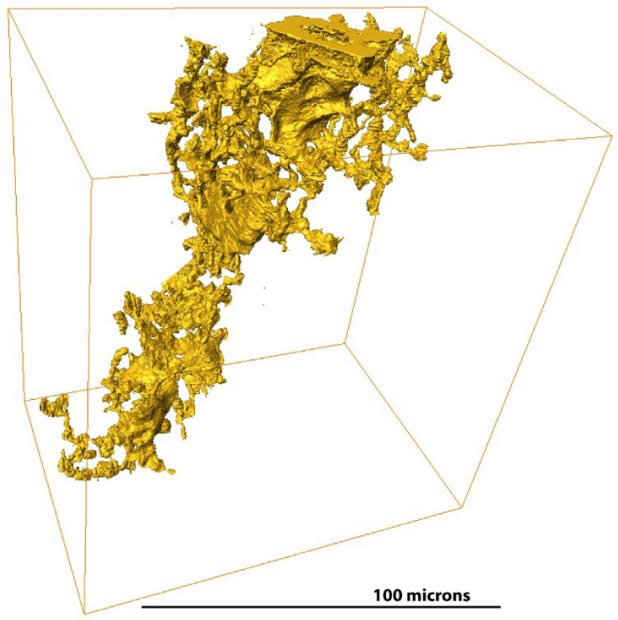

Fig. 9. 3D nanotomographic reconstruction of a deformation melt network. A. Reconstruction of the largest interconnected FeS melt accumulation within a small sub-volume of Cam3-FeOl1 (0.13 μm voxel size). This represents around 1/3 of the melt in the volume scanned (Full reconstruction shown in Fig. 9). Note fine sheets of melt joining larger melt accumulations. NB resolution is still too low to resolve the thinnest <0.1 μm melt networks observed in SEM analysis. Orientation as in Fig. 8.

Melt connectivity is thought to relate to melt geometry by concavity/convexity of a particle shape. A melt pocket of more convex nature is more likely to be isolated than a particle with a concave, more convolute shape, in essence describing the shape's specific surface area (Bear, 1972, p. 50). Therefore an important parameter to investigate is the relationship between melt pocket volume, and surface area, which can indicate how convex a shape is. This is particularly the case where thin melt sheets may be missed in segmentation that would otherwise connect two melt volumes. Individual analysis of melt pocket shape has been carried out using the Label Analysis feature on Avizo Fire™, and the in-built shape factor Shape_VA3d, defined as

$$Shape_{VA3d} = \frac{(Area3D)^3}{(36 \times \pi \times Area^2)} \quad (1)$$

where *Area3D* is the measured 3D surface area of the particle, and *Area* is the surface area of the particle shape cross-section. In this case, a higher value indicates a higher surface area to volume ratio and, therefore, a more concave or convolute melt pocket. Results are shown in Fig. 10 for all nano-XCT scans carried out, showing volume reconstructions of melt pockets filtered to ranges of Shape Factor (SV) value of <2, 2–10, and >10.

SV correlates well with visual appearance of melt pockets in SEM investigation and in reconstructed 3-D models. Shapes of factor 2 are convex and close to spherical. This category is inferred to represent stranded melt in tiny spherical melt pockets as observed in 2-D observations of deformed samples and in previous studies (Nichols, 1976). Those of SV >10 have more complex convolute shapes indicating melt sheets and tubes, that suggest interconnectivity across multiple olivine grains. Intermediate SV values of 2–10 represent relatively flattened melt sheets of intermediate size. By examining these intermediate melt pockets qualitatively, particularly in sample Cam3-FeOl1 which has been studied at multiple resolution, there appears to be a fabric produced by alignment of these melt sheets, which could reflect the overall sample fabric observed in micro-CT analysis. Although these melt pockets are isolated within the nano-CT reconstructions, it may be reasonable to assume, due to their shape, that they represent melt wetting grain boundaries and, therefore, that they have the potential to connect together with ongoing deformation/annealing.

As seen in Fig. 10, a correlation exists between melt pocket shape and volume in deformed samples, with near-spherical melt pockets being solely restricted to very small melt volumes, and more complex convolute shapes restricted to larger melt volumes. In contrast, the undeformed sample FeOlPC8 shows a weaker correlation, with larger melt volumes also having near spherical convex shapes. FeOlPC8 does not have any melt particles with a shape factor greater than 10, supporting the observation that the undeformed sample is made up of mostly high-dihedral angle, isolated melt pockets and that the percolation threshold is high in undeformed samples. The ultra-nano XCT scan of Cam3-FeOl1 has a similar melt geometry and texture to FeOlPC8, but the scale of individual melt pockets is in fact an order of magnitude smaller. This reflects the tendency for deformation to distribute melt more finely throughout the silicate matrix, following draining of melt from small volumes of the sample.

As nano-XCT gives a reliable measure of melt volume %, the fraction of melt within each shape category can be used to estimate the melt fraction within samples that is stranded in isolated near-spherical melt pockets in deformed vs. undeformed samples, as shown in Fig. 11. Results are normalised to a melt content of 4 vol% to take account for random melt distribution across the samples due to localised melt redistribution and allow inter-sample comparison. The relative proportion of small spherical pockets of melt in Cam3-FeOl3, Cam3-FeOl1 and the higher resolution (HR) scan of Cam-FeOl1 are all similar when normalised to the average melt content of the sample. Therefore the amount of melt that is isolated in small spherical melt pockets is similar across the samples, even though Cam3-FeOl3 and Cam3-FeOl1 HR scans do not have any larger melt veins present in the volumes analysed (i.e. melt is localised outwith the analysed volume). The undeformed sample shows a very different distribution, with >20% of total melt fraction found in pockets of near-spherical shape. Assuming that melt in near spherical (SF <2) melt pockets is isolated, and that melt in highly convoluted pockets (SF >10) are definitely connected across multiple grains, it can be inferred that the stranded melt fraction in deformed samples is approximately 0.5–2 vol%. Alignment and flattening of the intermediate geometry melt pockets within Cam3-FeOl1 suggests these melt pockets could become interconnected during prolonged annealing, and that the stranded melt fraction might be towards the lower end of this range.

Skeletonisation, in which melt networks are reduced to a series of 1-D branches and intersecting nodes, was used to quantify melt network connectivity in Cam3-FeOl1 compared to undeformed sample FeOlPC8. This was performed using the AVIZO Fire™ 8 Skeletonisation module, using default auto-skeletonisation settings and segmented melt fraction data from 0.13 voxel size. The single largest interconnected network from Cam3-FeOl1 (Fig. 9) was also examined individually to compare its connectivity to the full melt volume. The resulting topological spatial graphs were analysed for their branch length, thickness and volume. Cleaning of data and node connectivity analysis was carried out using SkeletonCleaner software (Ballhaus and Ellis, 1996; Miller et al., 2014; Zhu et al., 2011). An ideal, fully-interconnected melt network of tubules along triple junctions is predicted to have four branches per node (Von Bargen and Waff, 1986), although natural basaltic melt networks studied have an average closer to three, even at textural equilibrium, which may be in part an artefact of the skeletonisation process (Zhu et al., 2011). Fig. 12A and C show results of the skeletonisation of the FeOl1 nanotomographic dataset (full reconstruction), and undeformed sample FeOlPC8, respectively. The undeformed sample has a very low number of melt pockets within the volume scanned, and frequency of nodes is an order of magnitude lower than in the deformed samples. The undeformed melt pockets show the largest majority of individual dead-ends, as expected, and average connectivity (1.6) is lower than in the full network scan of the deformed sample (1.9). It may be that the connectivity is still over-estimated however, as a number of small dead-end melt pockets appear to have been removed as part of the skeletonisation process.

The full 3D dataset of deformed sample Cam3-FeOl1 (Fig. 12A) produces a skeleton with a majority of dead-ends, although one third of the nodes are three-fold connections. The average connectivity of 1.9 connections per node is slightly higher than in the undeformed sample. The measured connectivity is likely to be a lower estimate as very fine (<0.1 μm thickness) melt sheets connecting regions of melt are missed in the segmentation due to resolution limitations. The fully interconnected network (Fig. 12B) has a higher average connectivity of 2.4, with a majority of 3-fold coordination nodes present. The average connectivity is still lower than that in basaltic networks found by Zhu et al. (2011), but this

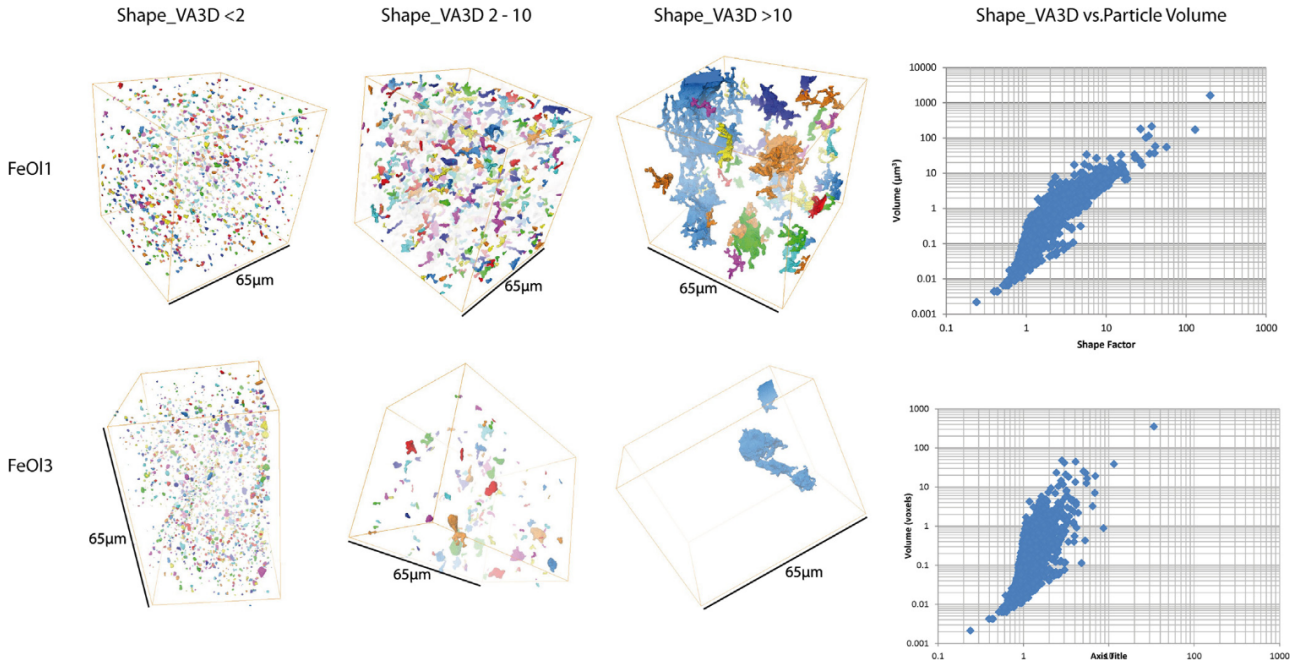

Fig. 10. Analysis of shape factor Shape_VA3d (Avizo Fire™) on nano-CT reconstructions of deformed samples. A: FeOl1 and FeOl3. For each sample, a volume rendering of segmented melt is shown which has a shape factor of <2 (left), 2–10 (middle), and >10 (right), and a plot showing relationship between segmented volume and shape factor (far right). Total melt fraction in FeOl1 is 4.1 vol%, in FeOl3 1.3 vol%; variation is expected as melt distribution is shown to be highly variable from micro-CT analysis. B: undeformed FeOlPC8, and ultra-high-resolution scan of Cam3-FeOl1 (15 μm field of view). Volume renders of particles with shape factors of <2, and 2–10, are shown, along with a graph of volume vs. shape factor for each sample. Both samples show a reduced range of shape factors compared to those of deformed samples in 11A. The UHR scan of FeOl1 represents an area that is relatively drained of melt, with melt taking up only 1.3 vol% of the total sample volume. In FeOlPC8 melt represents 2.7 vol% of total sample volume.

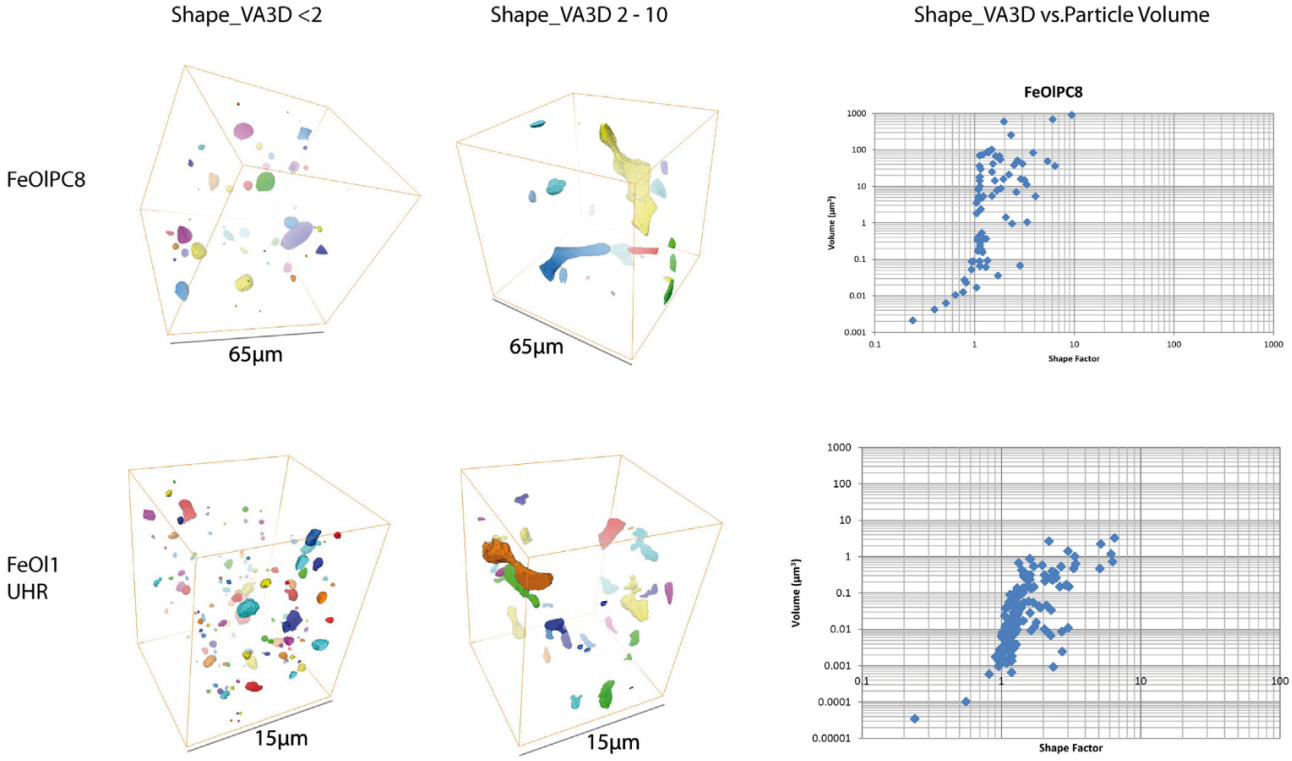

Fig. 10 (*continued*)

is expected due to anisotropy of the melt network. Only isotropic melt networks would be expected to show a 4-fold connectivity, as this represents a fully symmetric melt geometry.

The skeletonisation process also provides data on melt branch length and mean thickness, allowing a simple analysis of shape variation within a single segmented melt pocket/vein. The results shown in Fig. 13 highlight the geometric differences between melt in deformed and undeformed samples. In deformed samples melt is distributed across multiple branches creating a total length of branches that far exceeds the total length of the melt pocket, consistent with both visual examination of nano-XCT and 2-D SEM images.

The extent of connectivity of the large melt network in Cam3-FeOl1 was further tested by simulating fluid flow through a mesh created from volume renderings of the nano-CT data. Modelling was limited to qualitative results indicating relative velocity of

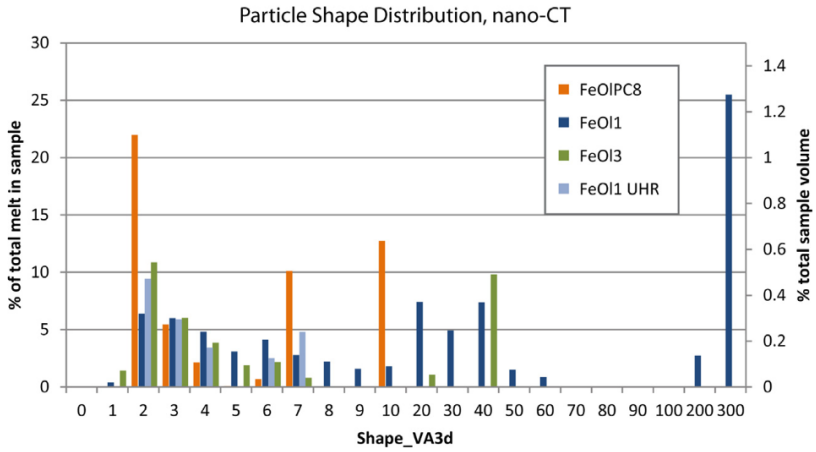

Fig. 11. Distribution of melt across pockets of varying shape within nano-CT reconstructions of experimental samples. Each sample is expected to contain 5 vol% melt on average. Melt proportions have been normalised to show the proportion of melt observed relative to this average melt content (left) and as a % of the total sample volume (this assumes the relationship between melt geometry and melt pocket volume is roughly constant across the sample). This allows a better comparison between the scanned volumes, which each have a different melt fraction due to random selection of volumes from samples with an inherent variability in melt fraction. It is clear that, despite only showing a small fraction of melt within samples Cam3-FeOl3 and Cam3-FeOl1 (ultra-high resolution), both samples follow the distribution of deformed sample Cam-3FeOl1, suggesting that a similar proportion of melt may be stranded in small isolated melt pockets. In each case the proportion of melt in near spherical melt pockets (2 or less) is less than 10%. In comparison, undeformed sample FeOlPC8 has >20% of melt in pockets of near spherical shape.

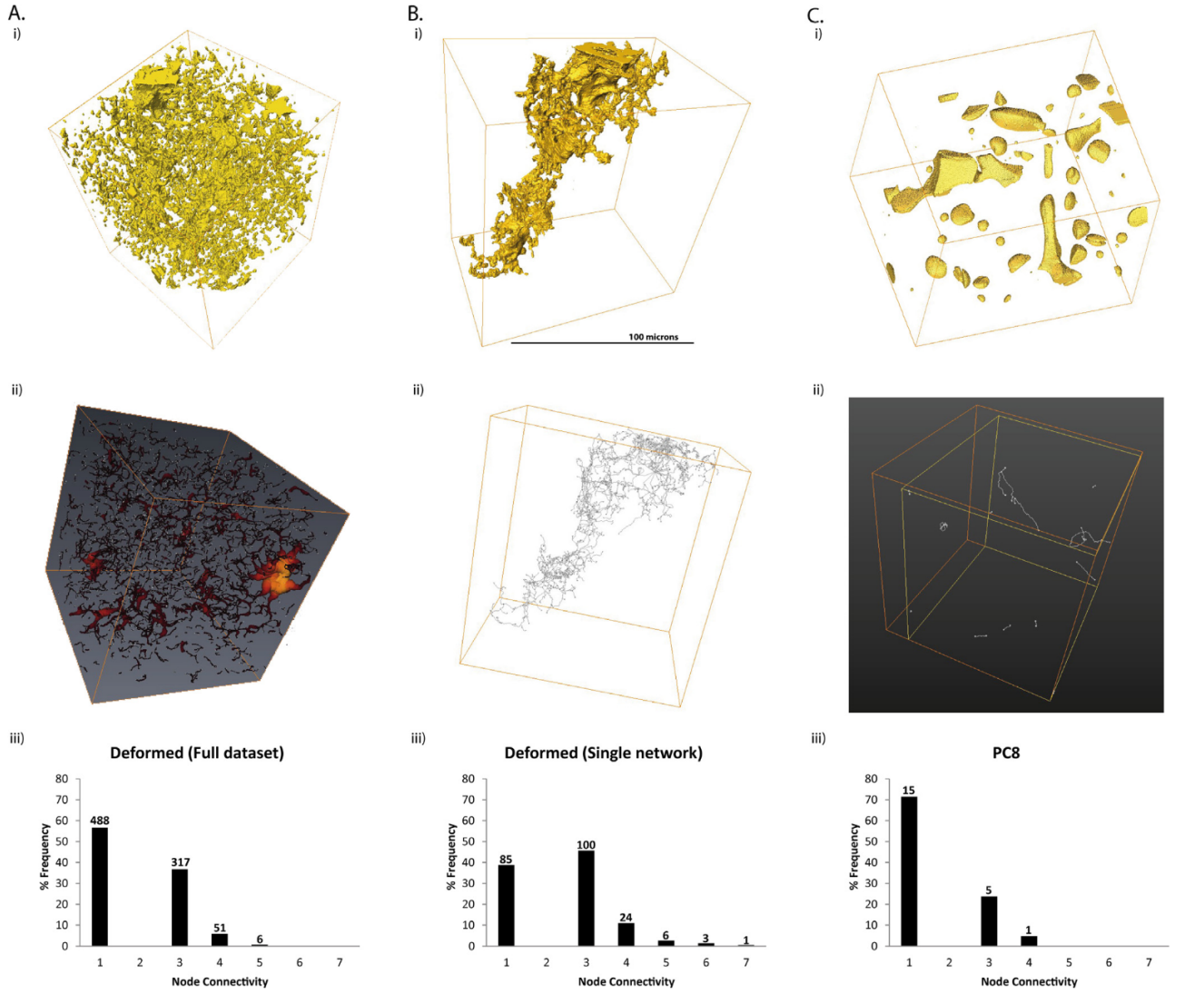

Fig. 12. Skeletonisation results. A. Deformed sample Cam3-FeOl1: full dataset. B. Deformed sample using only largest single interconnected network. C. Undeformed sampleFeOlPC8. In each case i) represents the original segmented dataset (melt rendered gold, olivine transparent), ii) represents the skeleton produced. The skeleton in A. also shows the average thickness of individual branches as calculated during the skeletonisation process. iii) Node connectivity vs % frequency of the skeleton networks as calculated from a 300×300×300 voxel region of interest.

fluid flow (further details in supplementary material). Fig. 14A shows the initial pressure gradient conditions input into the model, with resulting flow in the positive x direction (see axes in bottom left corner). Fig. 14B and C show the resulting flow pattern developed after a given time for melt flow. Modelling demonstrates that melt is able to move from one edge of the sample volume to the other in orthogonal directions. Preferred paths of melt flow indicate that melt is required to flow through fine sheets between grains and cannot bypass these through larger 3-grain boundary tubules, in contrast to results inferred from flow of basaltic melt within a similar olivine matrix (Zhu et al., 2011). This means fine sheets are likely to control permeability of the system. Although it is possible to conduct quantitative analysis by Lattice-Boltzmann modelling by refining the model used here, this was not attempted because it is clear that textures in deformed samples are transitory; as such, it is unclear how representative these results would be of melt migration within deforming melt networks. It may be possible to model flow by incorporating aspects of an evolving melt network within a deforming matrix (e.g. Rutqvist et al., 2002) although this is beyond the scope of this study.

3.4. Textural analysis of the olivine matrix

EBSD was performed on prepared sections of one undeformed sample (FeOlPC5), and three deformed samples (Cam3-FeOl1, Cam3-FeOl2, Cam3-FeOl4) to determine development of preferred crystal orientation in the olivine matrix. Interpretation was complicated by the orientation of cuts used for EBSD analysis, which varied across samples studied, as EBSD analysis was conducted following detailed XCT investigation and sectioning. Cam3-FeOl1 and Cam3-FeOl4 were analysed on their mid-section, while FeOl2 was examined on a planar section. This affects the orientation of deformation within the 2D section analysed. The results are discussed in detail in accompanying supplementary material and can be summarised as follows: 1) The undeformed samples show a very weak crystal preferred orientation (CPO) and some internal deformation of large crystal grains, probably due to slight axial compression of the samples during pressurisation. 2) There is a clear development of CPO in deformed samples, and evidence of dislocation creep in large grains. CPO development in small grains is most likely due to diffusion creep rather than dislocation creep under strain rates

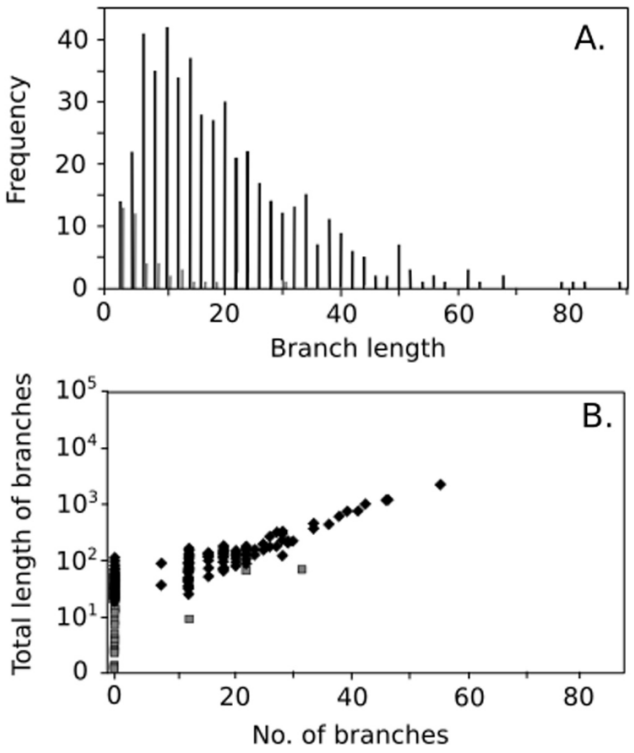

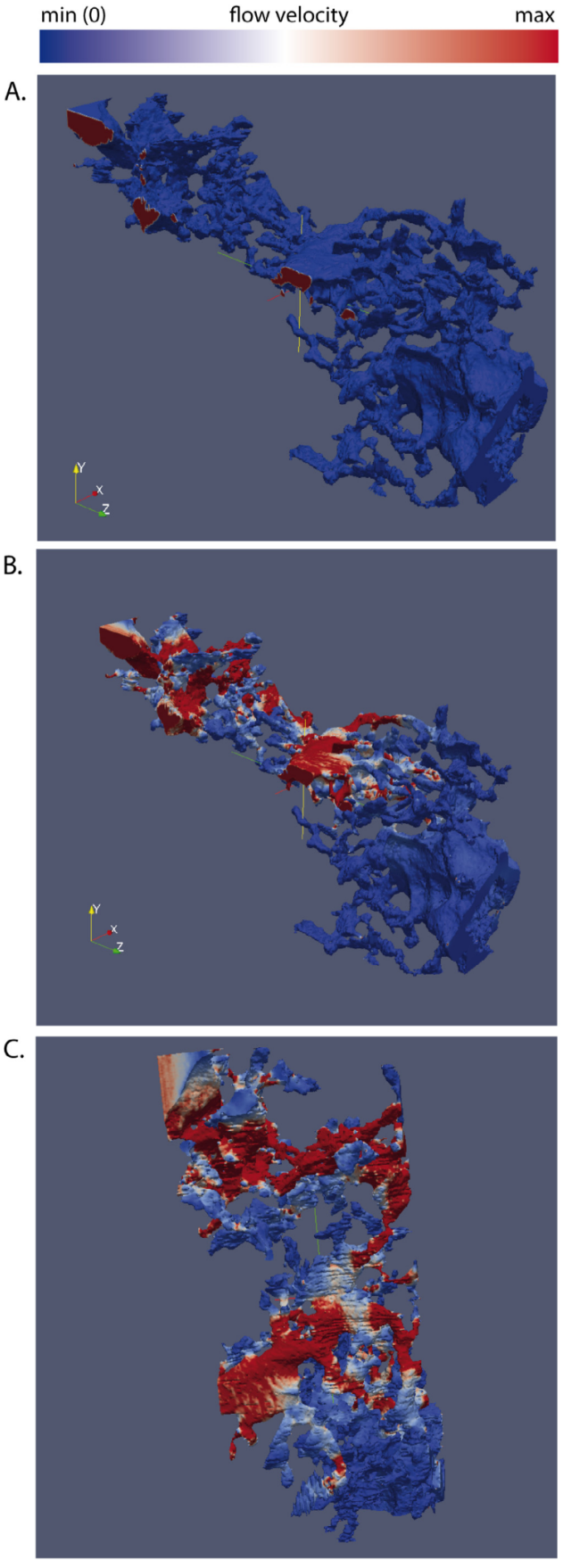

Fig. 13. Branch length analysis from skeletons of deformed and undeformed samples. A. Comparison of the distribution of branch lengths in the largest connected network of Cam3-FeOl1 (black lines), and the full FeOlPC8 segmentation (grey lines). Only the largest connected network was examined in FeOl1 because of the difficulty of processing all 1000 individual graphs to analyse mean length distribution. Branch length overall is much greater in the deformed sample, and the number of branches within the single deformed network is orders of magnitude greater than in the undeformed sample (made up of 18 individual isolated skeletons). This reveals the complexity of the deformed melt network, being made up of numerous larger melt pockets connected by wetted grain boundaries between numerous small olivine grains. B. Total number of branches in vs. total length of branches summed FeOl1 (black diamonds) and FeOlPC8 (grey squares). Total length of branches in the deformed networks is almost 2 orders of magnitude greater than the largest skeleton observed in the undeformed sample. Lengths are in voxels, each voxel representing a length of 0.13 μm.

used here (Miyazaki et al., 2013). However, an absence of in-situ stress-strain measurements makes this assertion tentative. 3) The CPO developed in response to deformation is likely to be consistent within deformed samples FeOl4, and FeOl2, but FeOl1 shows a different slip system active. It is unclear what causes the differences in CPO observed across deformed samples. Changes in strain-rate lead to different slip-systems being activated (Raleigh, 1968): CPO observed in FeOl1 may be consistent with the deformation pattern observed for systems with lower permeability (relative to basaltic melt + olivine; Holtzman et al., 2003), which would be expected in a system containing lower mobility FeS melt. The CPO development in the other deformed samples is not directly comparable to those observed in their study, or in fact any of the common slip systems of olivine.

Although EBSD analysis of samples is incomplete, and by necessity a minor component of the present study which is focused on textural development of melt networks, results do suggest that stress in samples is accommodated by both modification of Fe-melt networks and deformation of the solid silicate matrix. Further investigation of strain partitioning and deformation mechanisms in silicate-Fe melt systems is clearly required, as the presence of variable Fe-melt factions likely influences rheological response of

the entire system, which in turn has implications for modelling processes within rocky bodies during core formation.

4. Comparison to previous deformation studies

Detailed 2-D and 3-D analysis presented here support the assertion that deformation results in fundamental changes in texture in the Fe-S melt/olivine system, and that deformation aids Fe-melt percolation through solid silicate independent of strain rate. Textures in deformed samples are in some ways similar to those noted in earlier studies (Bruhn et al., 2000; Groebner and Kohstedt, 2006; Hustoft and Kohlstedt, 2006; Rushmer et al., 2005; Wang et al., 2011), with Fe-S melt visibly wetting silicate grain boundaries. However, melt channels developed in deformed samples are characteristically micron to sub-micron thick meandering melt bands which wet olivine grain boundaries. This is distinct from previously described textures where melt interconnectivity occurs due to alignment and merging of melt pockets. Although we observe localised melt drainage from volumes of deformed samples, evidenced by (1) distribution of very fine, spherical melt pockets which clearly contrast larger trapped melt pockets in undeformed samples, and (2) concurrent larger melt accumulations in deformed samples, we do not observe larger, segregated melt bands noted in previous studies. However, evidence of alignment of larger melt pockets in micro-CT data could indicate that at higher finite strains, greater melt interconnectivity might be expected, with the eventual channelization of melts into melt bands oriented at a shallow angle to the normal of the torsional rotation axis.

3-D visualisation clearly reveals that deformation enhances connectivity regardless of strain rate, despite a lack of strong melt preferred orientation fabrics. Absence of significant melt redistribution within samples may be due to the absence of sufficient gradients in pressure, temperature and/or stress, which would act as a driving force for melt migration. For example, in previous experiments conducted using simple shear deformation equipment and serrated pistons, regions of compression (high pressure) and tension (low pressure) were inferred to aid melt pooling in low-pressure regions (Hustoft and Kohlstedt, 2006). Our experiments demonstrate that grain boundary wetting is particularly pronounced at low strain-rates during prolonged annealing. In this respect our results contradict the findings of Walte et al. (2011), a study conducted at comparable P-T conditions and relatively low strain-rates. Walte et al. (2011) did not see evidence of stress acting to change textures in experimental samples at strain-rates of less than $10^{-4}\,s^{-1}$ in their deformed FeS-olivine samples. In our experiments we clearly see stress-dominated melt sheets, which are finer than 1 μm in our lowest strain rate ($10^{-6}\,s^{-1}$) experiment. Differences between the findings of this study and that of Walte et al. (2011) may be due to the longer experimental duration of our very low strain rate experiments, which could allow more time for samples to develop textures. However, this would imply that there was a significant kinetic control on the development of extensive micron-thick melt bands, especially the extensive melt channels observed in our lowest strain rate sample. Alternatively, differences between the two studies may also arise due to differences in experimental geometry: textures are likely to develop differently in the pure shear, axial compression experiments of Walte et al. (2011) compared to the simple shear in our torsion experiments (Kohlstedt and Holtzman, 2009 and references within). For example, pure shear may not encourage redistribution into melt-rich and melt-poor regions, as seen in geometries that apply significant simple shear deformation (Bruhn et al., 2000; Hustoft and Kohlstedt, 2006). However, it is clear that further investigation is required to determine the mechanisms for melt redistribution observed at high pressure and temperature.

Fig. 14. Results of computational fluid dynamics simulation of fluid flow through a binarised model of large melt network in sample Cam3-FeOl1 based on nano-XCT data. A. The initial boundary conditions showing max. Pressure at the X-origin plane. B. Flow conditions after a time x. Melt has flown through the melt network showing preferential high velocity fluid pathways in larger volume spaces. However, high velocities are also seen in very fine tubules and sheets, indicating melt is forced to flow through these fluid pathways; therefore permeability will be limited by these narrow bottlenecks. C. A view of the same flow in the Y direction showing the flow from X-min to X-max planes and flow through narrow melt pathways.

5. Extrapolation of results to core-forming conditions

Results from our experiments imply that application of differential stress enhances connectivity of FeS melt in an olivine matrix over a significant range of experimental strain rates. For this mechanism of deformation-aided percolation to segregate core and mantle material in rocky bodies in the early solar system it must be scalable to realistic conditions of planetary interiors. For core formation to be fully complete before the onset of silicate melting, melt must be able to drain from a silicate mantle to leave behind a fraction of 1 vol% or less in order to reproduce observed geochemical signatures (Groebner and Kohstedt, 2006), and be able to segregate melt over realistic timescales (Kleine et al., 2009). Previous studies have examined this process of extrapolation to investigate the potential efficiency of percolative core formation at realistic time-scales and strain-rates (Groebner and Kohstedt, 2006; Walte et al., 2011). Any extrapolation from laboratory experiments to core-forming conditions must take into account, 1) The significant reduction in strain rate, and therefore differential stress, acting on melt pockets at planetary conditions: deformation in proto-planets is expected at low strain rates due to convection (10^{-12}–$10^{-14}\,s^{-1}$, Walte et al., 2011), medium strain rate from potential tidal forces and high strain-rates in localised events from ongoing bombardment/accretion (10^{-11} to $>10^{-7}\,s^{-1}$, (Rushmer et al., 2005). Lowest strain rates in experiments are $10^{-6}\,s^{-1}$ (present study). 2) A significant increase in timescales under high P-T and exposure to differential stresses: core formation is likely to have taken place over millions to tens of millions of years (Kleine et al., 2002, 2009); in comparison laboratory experiments are on the time scale of hours to days. 3) The increase in grain size expected in planetary materials: grain size in planetary bodies is expected, from textural observations of meteorites, to be on the mm to cm scale (Mittlefehldt et al., 1998), compared to μm-scale in laboratory experiments.

The initial ability of deformation to create interconnected melt networks depends on the balance of differential stress, which acts to force melt out of isolated pockets and onto grain boundaries, and the interfacial tension between liquid melt and solid grain boundaries, which, as demonstrated in static experiments of Fe-rich melts, acts to isolate melt pockets at grain boundary triple junctions. Groebner and Kohstedt (2006) suggest that for deformation enhanced segregation to take place, the following inequality must be true:

$$\frac{\sigma}{\gamma_{s-l}/r} > 1 \tag{2}$$

where σ is the differential stress, γ_{s-l} is the interfacial energy between solid and liquid, and r is the melt pocket size. Groebner and Kohstedt (2006) proposed that the competing effects of increasing grain size and decreasing strain rate effectively cancel each other out, implying that conditions in deformation experiments

are actually directly analogous to those during core-formation. In contrast, Walte et al. (2011) suggested, on the basis of their study of olivine-Fe-rich melt and an analogue norcamphor-H_2O, that an additional scaling factor, R, is needed to describe the interplay between differential stress and surface tension:

$$R = \frac{\Delta P}{\Delta \sigma} \leftrightarrow R = \frac{2\gamma_{s-l}}{rA\dot{\epsilon}^{\frac{1}{n}}} \quad (3)$$

where ΔP is the melt pocket overpressure, $\Delta\sigma$ is differential stress, A is a temperature dependent pre-exponential factor, $\dot{\epsilon}$ the strain rate, and n the stress exponent in the stress-strain relationship for deformation. The value of R is inferred by Walte et al. (2011) from the relationship between melt pocket size and shape observed in their HPT and analogue experiments.

As previously discussed, our observations differ from those of both Walte et al. (2011) and Groebner and Kohstedt (2006). We see no dependence of deformation-aided melt segregation on experimental strain rate, consistent with the inequality given in [2], implying that additional scaling is not required to extrapolate data to lower (planetary) strain rates. However, this inequality assumes that melt shape instantaneously adapts to the ratio of surface tension and differential stress. Although we observe wetting of olivine grain boundaries and melt redistribution in all deformed samples, more extensive melt channels appear to be better developed in the longest duration experiment. A kinetic effect for textural development would be inconsistent with the equality given in [2]. The positive correlation between melt pocket radius and shape factor shown in Fig. 10 does support [2] because it implies that as melt pocket radius decreases, interfacial tension increases relative to differential stress. This is consistent with the observed trapping of submicron-sized melt pockets in volumes of deformed samples from which the melt has drained, although it is not consistent with the presence of sub-micron sized melt bands connecting smaller melt pockets. It is apparent from observations here that melt interconnectivity cannot simply be explained by a single physical model in which deformation results in near-instantaneous modification of melt pocket shape, and the eventual alignment of melt pockets to form interconnected melt bands. Rather, melt channels in deformed samples are micron to sub-micron thick channels which permeate the solid olivine matrix, occasionally resulting in the formation of larger ponded melt pockets. Additionally, alignment of larger melt pockets is also noted, possibly promoting additional melt interconnectivity at higher finite strain. As such, the inequality given in [2], or a modified version of this taking additional consideration of scaling effects, cannot readily be used to extrapolate textural development noted in experiments here to lower strain rates. Any scaling would require an alternative physical model for the formation of sub-micron melt channels, and consideration of the effects of any change in texture which might be noted with progressive annealing, such as the eventual formation of melt bands as noted in previous studies. However, we note that the observed independence of deformation-aided percolation on strain rate in the present study indicates that the mechanism cannot readily be discounted as a mechanism for core formation in terrestrial bodies, either at higher strain rates due to impact events, or at much lower strain rates due to convection processes.

6. The possibility and consequences of core formation without magma oceans

Textures observed in deformed samples provide clear evidence that deformation aids mobilisation of FeS melt within a silicate matrix, resulting in the formation of extensive, narrow melt channels and localised draining and accumulation of FeS melt. Previous experimental studies have also shown that metallic melt networks form at very high confining pressures (>50 GPa) (Shi et al., 2013; Takafuji et al., 2004), indicating that deformation-aided melt segregation might be further promoted at increased pressure. The volume of stranded melt in deformed samples here is estimated to be 0.5–2 vol%; this is considerably lower than that in undeformed samples, which on the basis of experiments performed here exceeds 5 vol%, and may be considerably higher. However, timescales for FeS segregation cannot readily be determined. FeS is observed to be locally drained from 10^1 to 10^2 μm^3 volumes of samples over the duration of experiments, but there is no evidence of net migration of melt, most likely due to the absence of significant gradients in pressure/temperature/strain within the samples. Clearly more work is required to determine timescales for metallic melt segregation by percolation and the contribution which this process may play in core formation prior to, or in the absence of extensive silicate melting in planetesimals and planets. However, although scaling of percolation processes to lower strain rates in planetary interiors is not straightforward, the observed lack of a dependence on strain rate suggests that deformation-aided percolation cannot be dismissed as an additional mechanism for core formation.

Earth's core and mantle are not currently at chemical equilibrium. However, a common assumption of many studies is that core formation via a deep silicate magma ocean would have resulted in liquid metal-liquid silicate equilibration under HPT conditions. Early core-formation by percolation raises the possibility that (1) a fraction of the Earth's core formed by percolation resulting in liquid metal/solid silicate equilibration or partial equilibration over a range of pressure-temperature conditions; and (2) that small planetesimals accreting to form the Earth had already fully or partially differentiated, resulting in metal-liquid/solid silicate equilibration at relatively low pressure/temperature conditions. Unless an extensive magma ocean existed on Earth for a very protracted period of time, or unless the entire silicate portion of the Earth was molten, it is unlikely that the chemical signatures of early core formation by percolation could be eradicated, and the geochemistry of Earth's mantle (and the mantles of other terrestrial planets) may instead record a complex, multi-stage process of core segregation. Rudge et al. (2010) have demonstrated that corresponding 'disequilbrium' or 'partial equilibrium' models can be used to explain key geochemical signatures which are commonly used to inferred timescales and processes of core formation during full chemical equilibration in a silicate magma ocean. As such, the key assumption of many studies of core formation, that liquid silicate and liquid metal were in chemical equilibrium at the base of a deep, evolving magma ocean (e.g. Wade and Wood, 2005; Wood et al., 2006), must be called into question. An important objective of studies of core formation should be modelling the effects of chemical disequilibrium, partial equilibrium, and liquid metal-solid silicate equilibrium into complex, multi-stage models of core segregation.

Acknowledgements

This work was supported by the University Of Edinburgh (Principal's Career Development studentship), the Natural Environment Research Council under NE/I016333/1, Science and Technology Facilities Council, European Synchrotron Radiation Facility, and the EPSRC for the Manchester X-ray Imaging Facility under EP/F007906/1 and EP/F028431/1. The authors would like to thank Nico Walte and an anonymous reviewer whose comments and suggestions improved this manuscript considerably.

Appendix A. Supplementary data

Supplementary data associated with this article can be found, in the online version, at http://dx.doi.org/10.1016/j.pepi.2017.01.004.

References

Bagdassarov, N. et al., 2009. Constraints on the Fe-S melt connectivity in mantle silicates from electrical impedance measurements. Phys. Earth Planet. Inter. 177 (3–4), 139–146.

Ballhaus, C., Ellis, D.J., 1996. Mobility of core melts during Earth's accretion. Earth Planet. Sci. Lett. 143 (1–4), 137–145.

Barrat, J.A. et al., 2015. Early stages of core segregation recorded by Fe isotopes in an asteroidal mantle. Earth Planet. Sci. Lett. 419, 93–100.

Bear, J., 1972. Dynamics of Fluid Flow in Porous Media. American Elsevier Publishing Company.

Bromiley, G.D., Hiscock, M., 2016. Grain boundary diffusion of titanium in polycrystalline quartz and its implications for titanium in quartz (TitaniQ) geothermobarometry. Geochim. Cosmochim. Acta 178, 281–290.

Bromiley, G.D. et al., 2009. A portable high-pressure stress cell based on the V7 Paris-Edinburgh apparatus. High Pressure Res. 29 (2), 306–316.

Bromiley, G.D. et al., 2010. Water incorporation in synthetic and natural $MgAl_2O_4$ spinel. Geochim. Cosmochim. Acta 74 (2), 705–718.

Bruhn, D., Groebner, N., Kohlstedt, D.L., 2000. An interconnected network of core-forming melts produced by shear deformation. Nature 403 (6772), 883–886.

Cerantola, V., Walte, N.P., Rubie, D.C., 2015. Deformation of a crystalline olivine aggregate containing two immiscible liquids: implications for early core-mantle differentiation. Earth Planet. Sci. Lett. 417, 67–77.

Craddock, P.R., Warren, J.M., Dauphas, N., 2013. Abyssal peridotites reveal the near-chondritic Fe isotopic composition of the Earth. Earth Planet. Sci. Lett. 365, 63–76.

Groebner, N., Kohstedt, D.L., 2006. Deformation-induced metal melt networks in silicates: implications for core-mantle interactions in planetary bodies. Earth Planet. Sci. Lett. 245 (3–4), 571–580.

Halliday, A.N., 2013. Earth science: small differences in sameness. Nature 497 (7447), 43–45.

Heilbronner, R., Barrett, S., 2014. Image Analysis in Earth Sciences, vol. 520. Springer-Verlag, Berlin Heidelberg.

Holtzman, B.K. et al., 2003. Melt segregation and strain partitioning: implications for seismic anisotropy and mantle flow. Science 301 (5637), 1227–1230.

Hustoft, J.W., Kohlstedt, D.L., 2006. Metal-silicate segregation in deforming dunitic rocks. Geochem. Geophys. Geosyst. 7, 11.

Kleine, T. et al., 2002. Rapid accretion and early core formation on asteroids and the terrestrial planets from Hf-W chronometry. Nature 418 (6901), 952–955.

Kleine, T. et al., 2009. Hf-W chronology of the accretion and early evolution of asteroids and terrestrial planets. Geochim. Cosmochim. Acta 73 (17), 5150–5188.

Kohlstedt, D.L., Holtzman, B.K., 2009. Shearing melt out of the earth: an experimentalist's perspective on the influence of deformation on melt extraction. Annu. Rev. Earth Planet. Sci. 37, 561–593.

Linnen, R.L., Keppler, H., 1997. Columbite solubility in granitic melts: consequences for the enrichment and fractionation of Nb and Ta in the Earth's crust. Contrib. Miner. Petrol. 128, 213–227.

Miller, K.J. et al., 2014. Experimental quantification of permeability of partially molten mantle rock. Earth Planet. Sci. Lett. 388, 273–282.

Minarik, W.G., Ryerson, F.J., Watson, E.B., 1996. Textural entrapment of core-forming melts. Science 272 (5261), 530–533.

Mittlefehldt, D.W., 1998. Non-chondritic meteorites from asteroidal bodies. In: Papike, J.J. (Ed.), Planetary Materials (36: Reviews in Mineralogy), pp. 4–195.

Miyazaki, T., Sueyoshi, K., Hiraga, T., 2013. Olivine crystals align during diffusion creep of Earth's upper mantle. Nature 502 (7471), 321–326.

Nichols, F.A., 1976. Spheroidization of rod-shaped particles of finite length. J. Mater. Sci. 11 (6), 1077–1082.

Raleigh, C.B., 1968. Mechanisms of plastic deformation of olivine. J. Geophys. Res. 73 (16), 5391–5406.

Ringwood, A.E., 1979. Origin of the Earth and Moon, vol. 295. Springer, New York.

Rudge, J.F., Kleine, T., Bourdon, B., 2010. Broad bounds on Earth's accretion and core formation constrained by geochemical models. Nat. Geosci. 3 (6), 439–443.

Rushmer, T. et al., 2005. Fe-liquid segregation in deforming planetesimals: coupling core-forming compositions with transport phenomena. Earth Planet. Sci. Lett. 239 (3–4), 185–202.

Rutqvist, J. et al., 2002. A modeling approach for analysis of coupled multiphase fluid flow, heat transfer, and deformation in fractured porous rock. Int. J. Rock Mech. Min. Sci. 39 (4), 429–442.

Sahijpal, S., Soni, P., Gupta, G., 2007. Numerical simulations of the differentiation of accreting planetesimals with Al-26 and Fe-60 as the heat sources. Meteorit. Planet. Sci. 42 (9), 1529–1548.

Shannon, M.C., Agee, C.B., 1996. High pressure constraints on percolative core formation. Geophys. Res. Lett. 23 (20), 2717–2720.

Shi, C.Y. et al., 2013. Formation of an interconnected network of iron melt at Earth's lower mantle conditions. Nat. Geosci. 6 (11), 971–975.

Takafuji, N. et al., 2004. Segregation of core melts by permeable flow in the lower mantle. Earth Planet. Sci. Lett. 224 (3–4), 249–257.

Terasaki, H., Frost, D.J., Rubie, R.C., Langenhorst, F., 2005. The effect of oxygen and sulphur on the dihedral angle between Fe-O-S melt and silicate minerals at high pressure: implications for Martian core formation. Earth Planet Sc. Lett. 232 (3–4), 379–392. http://dx.doi.org/10.1016/j.epsl.2005.01.030.

Terasaki, H. et al., 2007. Interconnectivity of Fe-O-S liquid in polycrystalline silicate perovskite at lower mantle conditions. Phys. Earth Planet. Inter. 161 (3–4), 170–176.

Touboul, M., Puchtel, I.S., Walker, R.J., 2015. Tungsten isotopic evidence for disproportional late accretion to the Earth and Moon. Nature 520 (7548), 530–533.

Von Bargen, N., Waff, H.S., 1986. Permeabilities, interfacial areas and curvatures of partially molten systems – results of numerical computation of equilibrium microstructures. J. Geophys. Res. Solid Earth Planets 236 (1–2), 78–95.

Wade, J., Wood, B.J., 2005. Core formation and the oxidation state of the Earth. Earth Planet. Sci. Lett. 236 (1–2), 78–95.

Walte, N.P., Becker, J.K., Bons, P.D., Rubie, D.C., Frost, D.J., 2007. Liquid-distribution and attainment of textural equilibrium in a partially-molten crystalline system with a high dihedral-angle liquid phase. Earth Planet. Sci. Lett. 262 (3–4), 517–532.

Walte, N.P. et al., 2011. Deformation of a crystalline aggregate with a small percentage of high-dihedral-angle liquid: implications for core-mantle differentiation during planetary formation. Earth Planet. Sci. Lett. 305 (1–2), 124–134.

Wang, Y. et al., 2011. In-situ high-pressure and temperature X-ray microtomography during large deformation: a new technique for studying mechanical behaviour of multi-phase composites. Geosphere 7, 40–53.

Watson, H.C., Roberts, J.J., 2011. Connectivity of core forming melts: experimental constraints from electrical conductivity and X-ray tomography. Phys. Earth Planet. Inter. 186 (3–4), 172–182.

Wood, B.J., Walter, M.J., Wade, J., 2006. Accretion of the Earth and segregation of its core. Nature 441 (7095), 825–833.

Wood, B.J., Wade, J., Kilburn, M.R., 2008. Core formation and the oxidation state of the Earth: additional constraints from Nb, V and Cr partitioning. Geochim. Cosmochim. Acta 72 (5), 1415–1426.

Yoshino, T., Walter, M.J., Katsura, T., 2003. Core formation in planetesimals triggered by permeable flow. Nature 422, 154–157.

Zhu, W.L. et al., 2011. Microtomography of partially molten rocks: three-dimensional melt distribution in mantle peridotite. Science 332 (6025), 88–91.